Evidence and Quantification of Ion Migration in $MAPbBr_3$ Microcrystals via Local Photocurrent Measurements

Pedro De Oliveira[1,2], Tony Song[1], Bob Wang[1],
Qiaochu Wang[1], Yuqing Zhu[1], Henry Travaglini[1], Dong Yu[1]
[1] *Physics Department, University of California, Davis*
[2] *Physics Department, Cornell University, Ithaca*
(Dated: 31 of Janurary 2023)

We demonstrate the existence of ion migration in $MAPbBr_3$ microcrystals from 300 K down to 140 K through scanning photocurrent microscopy (SPCM). These microcrystals present no surface treatement, and discern from previous studies done on polycrystalline or large single crystal samples for its nature and size. From there, we propose that SPCM can still be used to quantify the mobility of ions or vacancies in the material by observing their effect on band bending and, ultimately, extracting an activation energy. We find an activation energy of 0.083 ± 0.009 eV for our samples. This value is significantly lower than those found for $MAPbI_3$, but can be explained due to the nature of our microcrystals with high free surface area. The study raises possible issues for size decrement of single crystal organic-inorganic perovskites in applications where ionic migration and hysteresis are detrimental.

I. INTRODUCTION

Organic–inorganic hybrid perovskite (OIPs) crystals have emerged as promising materials for photovoltaic applications and solid state devices. Their intrinsic long carrier diffusion lengths and recombination lifetimes relative to other conventional semiconductors [1–3], have shaped the path to the achievement of high light power conversion efficiencies (PCE), with recent 25.6% PCE in perovskite cells [4] and 32.6% PCE for perovskite and Si hybrid tandem cells [5]. Alongside photovoltaics, perovskites have potential applications in memory devices [6], and diodes [7].

Despite all the benefits, OIPs encounter difficulties amongst their semiconductor counterparts due to their instability for extended periods of time and in harsher environmental conditions, as in increased temperatures [8] and humidity levels [9]. However, one of the main challenges facing OIPs research and development is the presence of hysteretic behavior of current-voltage relation [10] and photocurrent measurements [11], see Fig 1. The hysteresis hinders steady-state operations of perovskite based devices, precise control of their optoelectronic properties, and further diminishes PCE's of their photovoltaic applications. It is, then, crucial to understand the underlying physics and chemistry that gives rise to this major weakness in order to, one day, circumvent it.

Many origins for this hysteretic effect have been suggested [10, 12–14], but it is important to highlight two specific ones: increased defect density at the surfaces and interfaces with other materials, and vacancy and/or mobile ion migration through the lattice. Diffusion of ion species has been pointed to cause unique phenomena occurring in OIPs, including the giant switchable photovoltaic effect [15] and the presence of a giant dielectric constant [16]. Many of the theoretical aspects of OIPs, specially ion migration, is poorly understood due to the difficulties created by breakdown of the Born-Oppenheimer approximation [17], complex phase transitions of first and second order [18], and interplay of various magnetic and ion induced effects [15, 16, 19, 20]. Experimental work on these systems can shed light on the underlying principles for the complex OIPs. The work presented here sets to quantify the effect of ion migration in the OIP material, $MAPbBr_3$.

A. Lattice Structure and Band Gap

The OIP family has compositional ABX_3, where A is an organic cation located in a cubo-octahedral lattice and contained within a BX_3 octahedral cage, B is a smaller inorganic metal cation, and X is a halogen. In this paper, we investigate $MAPbBr_3$, whose organic cation (MA) is methylammonium (CH_3NH_3), the metal cation is lead, and the halogen anion is bromine (Fig. 2). It is important to keep in mind that $MAPbBr_3$ exhibits four crystal phases depending on temperature: cubic (Pm3m, T > 230 K), β-tetragonal (I4/mcm, 230 K > T > 155

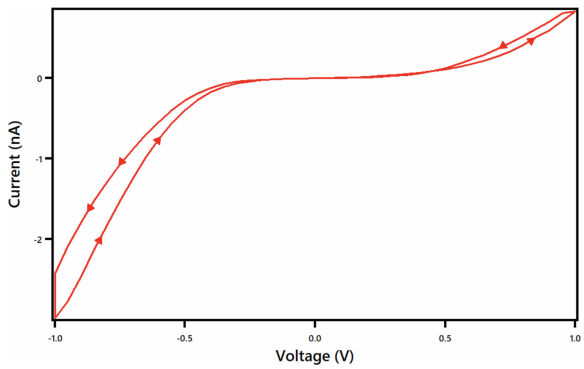

FIG. 1: Hysteretic IV curve of $MAPbBr_3$ for voltages swept between -1V and 1V, with rate 300 mV/s.

K), γ-tetragonal (P4/mmm, 155 K > T > 149 K) and orthorhombic (Pna21, T > 149 K) [18, 21, 22].

Electronically, $MAPbBr_3$ has a bandgap of $E_g \approx 2.3$ eV, corresponding to a photon of 539 nm wavelength, green color of the visible light spectrum. This makes this material particularly attractive for hybrid solar cells, given that it absorbs more efficiently higher energy photons around 2 eV compared to Si, and thus, thrive in conjunction [23, 24].

B. Ionic Transport

One of the main problems in the OIP functioning are the existence of intrinsic defects and vacancies in the lattice. Studies have shown that these vacancies have intrinsic characteristic of Schottky or Frenkel type [25], in which, pair wise ionic (a cation and an anion) vacancies are created, or misplacement of an ion from a lattice point to an interstitial site occurs, respectively. These vacancies, just as holes, have an effective local charge and, thus, affect the local electrical field. Although, extremely dependent on the process of fabrication of samples, and its consistency, ionic conductivity lies at the order of 10^{-8} S cm^{-1} for the more investigated cousin of $MAPbBr_3$, $MAPbI_3$ [20, 26–28]. These vacancies hop from site to site and move across the sample, pulling clouds of intrinsic electronic carriers with them, and therefore, "terraform" the local electrical field. This electrical field change, can, thus, be idealized to measure several properties of the ion transport. Examples of these mechanism include transient capacitance [29], photoluminescence [27], and resistance measurements [30].

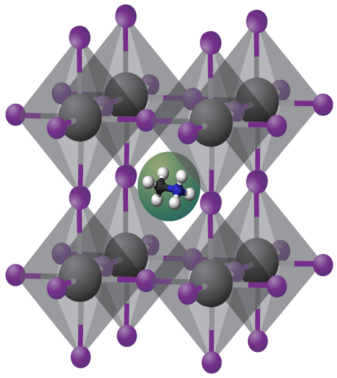

FIG. 2: Conventional cell for $MAPbBr_3$ for cubic crystal phase. The methylammonium stays in the center of a lead bromide cage, which confines it. The lead, in gray, is itself confined by 6 bromine atoms, in purple. The lead and the methylammonium form, each, a simple tetragonal lattice, meanwhile the bromine atoms are arranged as an edge centered tetragonal lattice. Note that the lattice is tetragonal only for temperatures between 230K and 149K, above which the lattice is cubic and below which the lattice becomes orthorhombic [18, 21, 22].

Although the theoretical details of ion transport paint an incomplete picture due to a multitude of possible effects, several attempts have been made to predict the activation energies for the different structures of OIPs. Models that idealize DFT often take a mean-field potential approach to estimate the migration path of vacancies between adjacent sites, thus, predicting the minimum necessary energy to activate such hopping [14, 31]. Others characterize these systems through molecular dynamics simulations [32]. The common theme of all these models is to characterize the activation energy for the hopping of vacancies between nearest sites.

The activation energy is the energy for the vacancy to move between nearest neighboring sites, but can be thought as the ion equivalent of the band gap energy used in semiconductor physics, and arises from the use of Boltzmann-Maxwell statistics. The ion conductivity, for a specific species, can, then, be expressed using Nernst-Einstein relation and with the use of Arrhenius law as,

$$\sigma_i = \frac{Z_i e^2 N_A C_{V,0} D_{i,0}}{k_B T V_m} \exp\left(-\frac{S_V}{k_B} - \frac{E_A}{k_B T}\right), \quad (1)$$

where we have used Z_i for the ion charge number, N_A as Avogadro's constant, V_m for the molar mass of perovskite, T for the temperature, e for the elementary charge, k_B for Boltzmann's constant, $C_{V,0}$ for the intrinsic defects' concentration as $T \to \infty$, $D_{i,0}$ for the species' diffusion coefficient as $T \to \infty$, S_V for the creation entropy of the vacancy site, and E_A is the activation energy [33–35].

With the use of conductivity measurements, one can measure this activation energy (often it is actually referred to as the activation enthalpy of migration). When comparing activation energies for multiple ion species, one general conclusion is that halogen vacancies account for most of the ion diffusion in perovskites, with a lower activation energy compared to a relatively immobile lead and MA matrix [14, 31, 32]. Studies done in $MAPbI_3$ systems find values around $E_A = 0.08$ eV for iodine vacancies [14, 34, 36] , although others report higher values of $E_A = 0.58$ eV for such vacancies [31]. Curiously, theoretical studies suggest that insterstial ions have higher activation energies than vacancies (against most DFT results), with $E_A = 0.159$ eV [32] or $E_A = 0.19$ eV [37]. Although most results pertain to $MAPbI_3$, we should expect similar reports for $MAPbBr_3$ due to the similarities between the systems [14]. We postpone the discussion the experimental findings on $MAPbI_3$ alongside our own results in $MAPbBr_3$.

We, then, propose a new method for measuring this activation energy through photocurrent measurements that probe local internal electrical fields of the material. This opens the possibility of extraction of an important material parameter, via an important experiment set up, scanning photocurrent microscopy (SPCM).

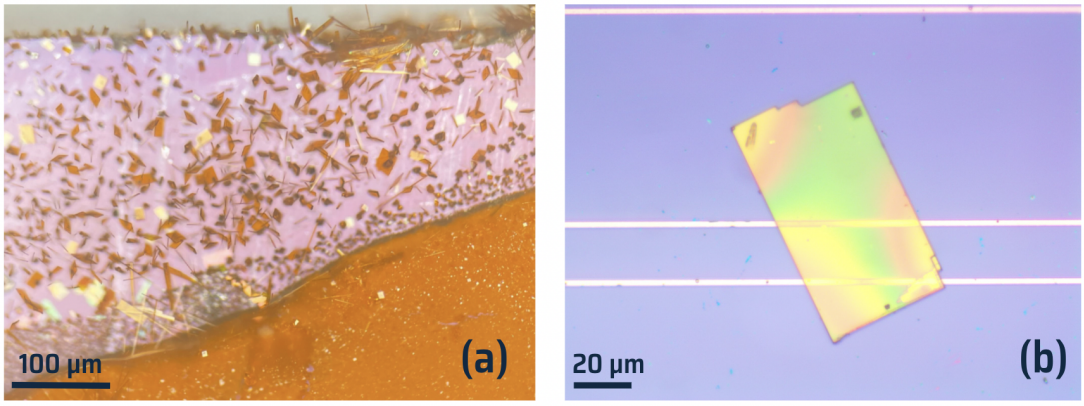

FIG. 3: **(a)** Picture of fabricated $MAPbBr_3$ microcrystals, each of these are then picked from the glass slide with the use of a cat hair. **(b)** $MAPbBr_3$ microcrystal on top of the gold electrodes, note that the distortions of color on the crystal represent the possible height variation.

II. METHODS

A. Device Fabrication

The device fabrication is outlined as in [38]. After the samples are fabricated, Fig. 3a, they must be transferred to a Si substrate chip covered by 300 nm SiO_2 and prepatterned with 5 nm Cr / 295 nm Au contacts, each pair having 10 μm or 20 μm separation, see Fig. 3b. The $MAPbBr_3$ microcrystals are transferred to the chip with the use of a cat hair, and then pressed into the electrodes for good contact. Due to the transferring methods and the variation of thickness within individual crystals, our devices often present better contact with one electrode than the other, making them asymmetrical. This fact has little effect, however, on the quantitative and qualitative assessments made in this paper. These gold contacts are used as the device's anode and cathode.

B. Measurements/Setup

The first set of measurements were KPFM measurements (Kelvin Probe Force Microscopy), performed on Veeco Dimension 3100. KPFM idealizes an AFM (Atomic Force Microscope) machine by applying a set AC voltage to the cantilever tip. The measured amplitude changes (AM mode) in the cantilever's oscillation according to surface potentials. The KPFM, thus, allows for direct visualization of the position dependence of surface electric potentials in semiconductor materials due to applied biases or band bending at device interfaces [39, 40]. A dehumidifier attempts to slow the degradation effects of water vapor on the $MAPbBr_3$ microcrystal, given that our AFM device operates under ambient pressure/air. In order to observe the time dependence of the electrical surface potential, we park and scan a single line continuously along the current flow direction every 10 seconds. Given most of the current channels through the lower end of the device (due to bottom contacts) and KPFM's inability to measure potential contributions much below the surface, lower voltages present little to no change on the scan. Therefore, we apply a 3V bias to the sample during scans. The prolonged high voltages per unit volume often damage the flake permanently.

The main results from this paper come from scanning photocurrent microscopy (SPCM). These optoelectronic measurements were performed at oblique incidence using a 532 nm continuous wave laser focused by a $10\times$ N.A. 0.25 objective lens. A pair of mirrors mounted on galvanometers raster scan the laser spot across the entire device, meanwhile photocurrents are measured as a function of laser position through a DL1211 preamplifier followed by a LabView data acquisition board. This light has enough energy to create excitations within the $MAPbBr_3$ flakes, whose bandgap corresponde to 539 nm light, making it ideal for the study of their electrical properties.

SPCM works on the simple principle that by shinning light into the material, an electron and hole pair is created. If the material is not intrinsic, the simple imbalance between mobility of the majority and the minority carriers create a local charge imbalance, and, therefore, an electrical field. If an additional electrical field, possibly due to band bending at interfaces/junctions or a bias, is present, the hole and the electron can reach the contacts where they may jump from the semiconductor to the metal [41]. This not only allows us to simply observe internal local electrical field, but gives us direct observation of the band behavior inside the material as a function of position, time, photon polarization and other parameters.

In our SPCM measurements, we place the sample with its wires within a cryogenic pressurized optical chamber. The chamber is, then, pressurized to approximately 10^{-6} Torr, and cooled with liquid nitrogen to the appropriate temperature. The procedure for data taking is as follows: we first turn on a positive bias of 1V, and take

the measurements during a 10 minutes period. Then, we turn off the bias and take data of relaxation for 20 minutes (we note that this will take longer since the only current is diffusive and does not include much drift). We change the bias to negative of same magnitude, and observe the effect for 10 more minutes. Finally, we observe relaxation once again for 20 minutes. We repeat the procedure at each temperature point. Due to the length of each measurement, and the fluctuation in the temperature controller (of 5 K), we opted to taking data at the following temperature points: 140 K, 180 K, 200 K, 225 K, 250 K, 275 K, 300 K.

III. RESULTS AND DISCUSSION

A. SPCM measurements

The obtained photocurrent maps are as presented in Fig. 4 for the control. We then select a line perpendicular to the contacts and observe the photocurrent evolve with time in order to look for ion migration evidence. Schottky barriers, that is, the bending of conduction and the valence bands at the depletion zone, causes charge separation, leading to photocurrent peaks. These peaks for the control stay close to their original value, and vary negligibly on the scale of ≈ 10 min. Given that the middle of $MAPbBr_3$'s band-gap lies approximately at 5.5 eV [23, 24], that our crystals tend to have p-type characteristic [38], and that pure gold has a work function of 5.1 eV (and lowers as gold gets contaminated [42]), the perovskite's band is expected to bend down at the interface with the gold, providing a barrier for the majority carriers, the holes. The control experiment confirms this hypothesis by demonstrating a positive peak at the biased electrode and a negative current peak at the ground/preamp electrode, corresponding to falling electrons. The observed asymmetry between the peaks may be attributed to the difference in contact resistance of the gold and $MAPbBr_3$, naturally arising from our transferring process.

When applying a bias, the electrical field creates a gradient on the band, and therefore accentuates or decreases the band bending near the electrodes. It is important to note that the configuration of preamp/GND and V_{bias} electrodes are kept the same throughout the whole experiment and can be seen at Fig. 4. At positive bias, see Fig. 5, the voltage reverse biases the V_{bias} electrode, while the electrical field magnitude decreases (just by superposition of potentials) near the GND electrode. This creates a spike of photocurrent at the biased electrode, which, due to the long diffusion lengths the crystal, overwhelms any of the negative contributions from the GND electrode. When the bias is negative, a seemingly reflected trend appears: the situation is equivalent now, but for holes. The holes move towards the V_{bias} electrode, and create a negative peak, see Fig 6. In terms of band bending, it can be understood by forward biasing the electrode enough to convert the downwards bend to an upwards bend. Meanwhile, the bending near the GND electrode increases in magnitude, but the trend is mostly unaffected there.

Upon careful analysis of the 1V versus -1V bias cases, some differences appear: (1) the maximum of the 140 K and 200 K peaks have roughly twice the magnitude in the negative case when compared to the positive case; and (2) a secondary photocurrent bump occurs at negative bias (see the 300 K plot), but is missing from the positive bias traces. Both can be explained with facts already mentioned. The first point arises, and can also be taken to be proof thereof, from the majority carriers being holes (p-type material). Having higher mobility and concentration, holes can move faster and in higher amounts to the electrodes, justifying (1). The second point arises as a result of p-n band bending behavior at the interface between perovskite and gold, respectively. The GND electrode is left mostly unaffected by the negative bias, and most electrons, traveling along the constant electrical field in channel, can fall into the gold. This results in a persistence, if not relative strengthening, of the negative peak at the GND electrode. This smaller peak surpasses the bias electrode after the manifestation of ion migration at 300 K, demonstrating its existence. This does not occur at 1V, since the GND electrode's bending is weakened.

Universal trends also appear: (1) the evidence of ion migration, (2) and the saturation thereof, as well as (3) temperature dependence. We attribute the decay of each peak to the migration and accumulation of ions, or their respective vacancies, near the electrodes. The mechanism of interaction between the band bending and ions works on the principle that the electronic movement time scale is much smaller than the ionic movement time scale, that is $t_{elec} \gg t_{ion}$. As ions migrate, electrons and holes reconfigure accordingly. The other assumption is that pure electronic behavior hardly affects the ionic movement. Therefore, the simple picture has the ions moving due to the electrical field in channel. Given that the ions cannot easily jump into the gold, they accumulate and bring with them a cloud of electronic carriers of opposite charge. The result is an effective p-doping of the region near the positive bias, or an effective n-doping near the negative biased electrode. The n-doping, or p-doping, screens some of the internal electrical field, and diminishes the effect of the forward or reverse bias, respectively [15]. Altogether, it decreases the electrical field near and between the electrodes, leading to the decays in Figs. 5 & 6. Point (2) emerges from the equilibrium between the diffusive and the drift forces for each ion species. Finally, point (3) is intuitive when thinking about semiconductor physics. The attempts at escape for each ion during its movement occurs at a rate (Γ) following Arrhenius law, that is $\Gamma \propto \exp(-E_A/k_BT)$, thus as temperature decreases, so does ionic movement.

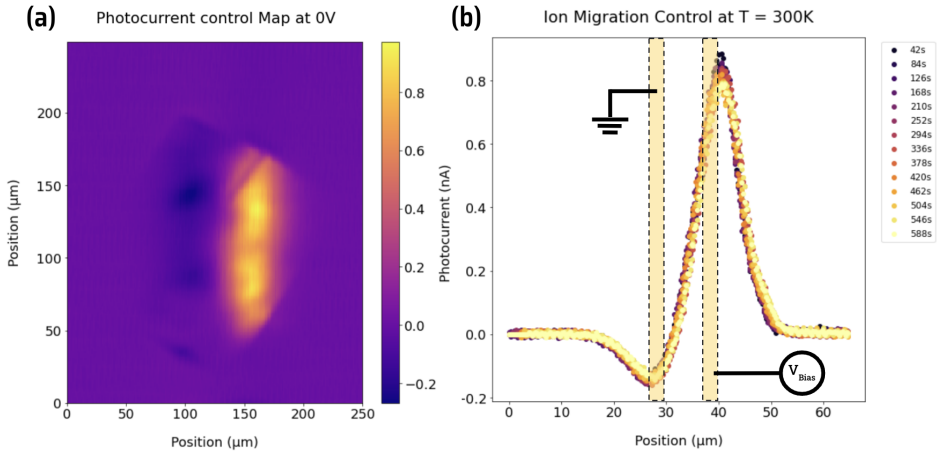

FIG. 4: Control Photocurrent Measurement at 300 K of $MAPbBr_3$ microcrystal. **(a)** Whole crystal map, from which we select one line to analyze its time evolution. **(b)**Photocurrent line trace of sample under no bias. The orientation of preamp and ground electrodes is as shown in the figure, and kept constant throughout the experiment.

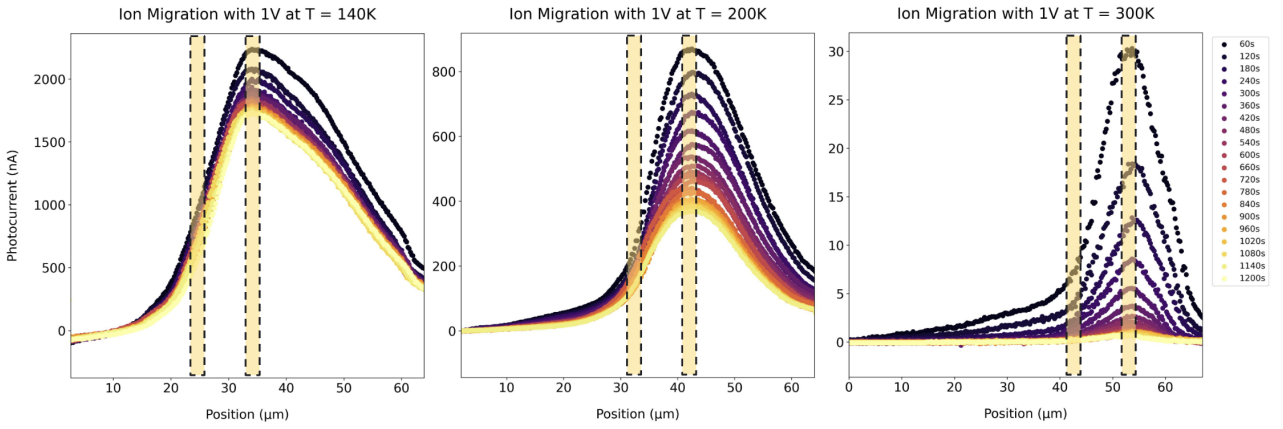

FIG. 5: Photocurrent Measurement Traces under an 1V Bias. From left to right, we select three representative temperatures, 140 K, 200 K, 300 K. These demonstrate the general trend as temperature increases. The gold contacts are biased as represented by Fig. 4's schematic, they are located 10 μm apart. The temperatures may oscillate within 5 K.

B. Extracting Activation Energies

The extraction of activation energies go beyond a qualitative assessment. The quantity extracted for this purpose was the decay time constant. We select the peak point of each photocurrent line scan and observe its change in time (note that the measurement at -1V bias and T = 300 K is treated as a special case for the point selection). The results are plotted in Fig.7. The data from 275 K for -1V and 1V bias are omitted, given that it presented major fluctuations due to external factors; time constraints set by the sample's degradation and difficulty of experiment made it challenging to acquire additional data. It is striking that if the negative bias curves are horizontally reflected and shifted by a constant y-offset all the curves overlap with their respective temperature positive bias curves, accordingly, almost overlapping completely at all times greater than 150 seconds. It demonstrates that ion migration is mostly unaffected by the direction of the bias.

A simple model that encapsulates the ionic movement in the material is described by the continuity equation,

$$\frac{\partial n}{\partial t} = \mu E \frac{\partial n}{\partial x} - D \frac{\partial^2 n}{\partial x^2}\,, \tag{2}$$

where $n(x,t)$ describes the vacancy/ion density, E is the in-channel electric field, μ is vacancy/ion mobility, and D is their diffusion coefficient. Separation of variables (on appropriate initial conditions) gives $n(x,t) \propto \exp(\pm t/\tau)$, where $\pm$ corresponds to positive or negative current peaks, respectively. Given that our electrical field peak depends on the concentration of ions, the evolution of the peak's maximum magnitude point is fit with the function $f(t) = C\exp(\pm t/\tau)$ in order to extract τ. This is

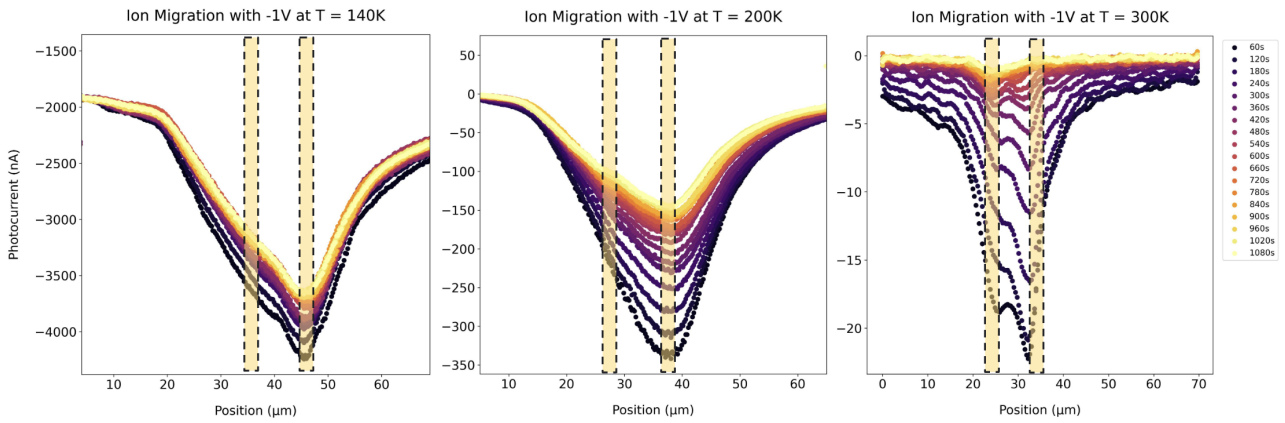

FIG. 6: Photocurrent Measurement Traces under an -1V Bias. From left to right, we select three representative temperatures, 140 K, 200 K, 300 K. These demonstrate the general trend as temperature increases. The gold contacts are biased as represented by Fig. 4's schematic, they are located 10 μm apart. The temperatures may oscillate within 5 K.

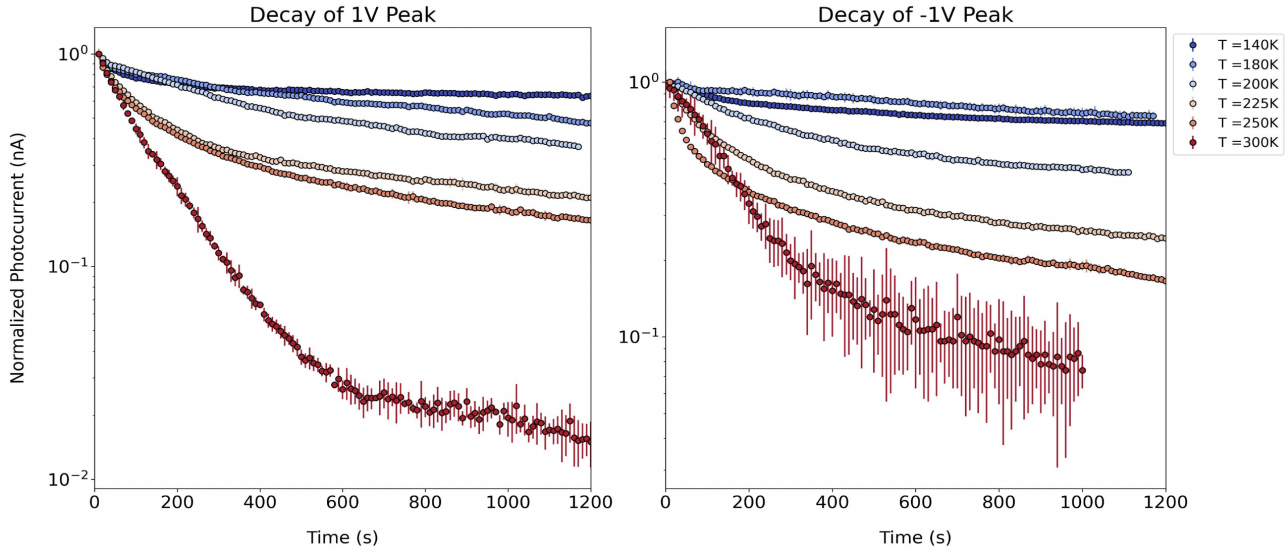

FIG. 7: Decay of peak points from SPCM trace measurements. Plotted in log scale in order to highlight the exponential trends. **Left:** Decay curves for the peak under a 1V bias. **Right:** Decay curves for the peak under a -1V bias. The uncertainties in the graph are found by going ±5 data points from the maximum magnitude point of each scan, these gives an estimate of uncertainty for the value at the electrode.

not as straightforward as it seems. Indeed, upon further thought, one should not expect the electrical field outside the contacts to decay due to ion migration, since, by the argument given in section III.A, the ions or vacancies should not dislocate themselves in that region. However, that is what we observe in Figs. 5 & 6. First, the assumption that the electrical field is zero outside of channel does not hold when the contact resistance is small [43]. Secondly, we may attribute this change to the vertical movement of ions. The crystal has some finite thickness that cannot be considered negligible, at the same time, the contacts are placed under the sample. This implies that the electrical field is not evenly distributed in the y-direction. The existence of a potential difference between the top and the bottom layers, creates ion movement in the y-direction. This movement reaches equilibrium faster than the x-directional movement, as the sample's thickness is less than the channel length, $y_0 < x_0$. This combined movement of ions in the x and y direction should take place in the early hundreds of seconds. The KPFM data confirms this idea (Fig.8); the left-hand-side out-of channel sample region generates an electrical field following 150 seconds. Note that the effects of this horizontal migrations on KPFM data reaches steady state faster than in the SPCM, arising from the KPFM's limited measurement to the top-

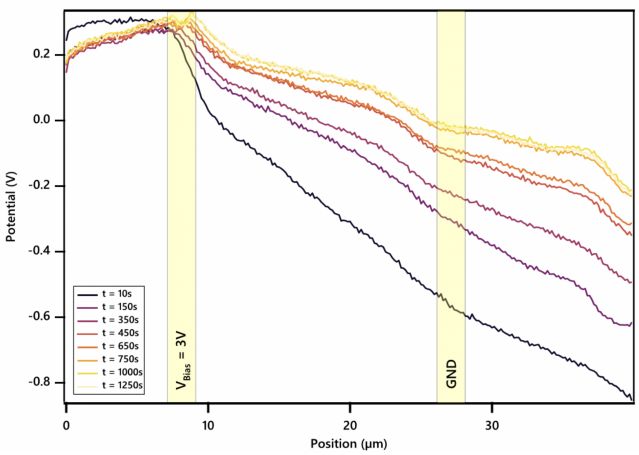

FIG. 8: KPFM mapping of the surface potential of $MAPbBr_3$. This data was taken with a 3V bias, with the electrode configuration as in the figure. Data taken for $\approx$ 20 minutes.

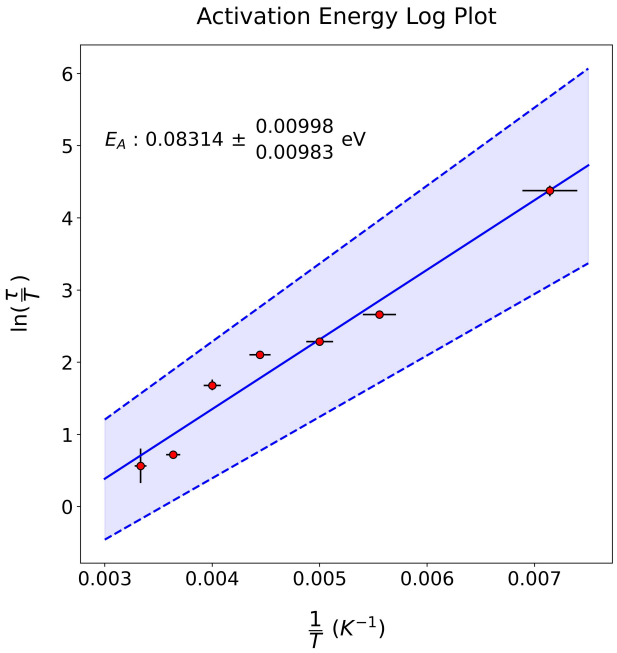

FIG. 9: Activation Energy Log Plot. We plot $\ln(\tau/T)$ vs $1/T$ in order to extract the slope of the linear fit as the activation energy. The region shaded in blue represents the area, where any line that stays inside can be considered a possible line of fit. The dashed line at the borders of the shaded region represent the boundaries of this uncertainty.

most layer of the crystal, meanwhile the laser of SPCM is able to penetrate it. The persistent electrical field on the right-hand-side region of the sample demonstrates that electrical fields are not exclusive to in-channel region.

Closer inspection of photocurrent Figs. 5 & 6, demonstrates the settling of out of channel decay at approximately 300 seconds after the start of measurement, with exception of 300 K data at 1V, which has a switch at approximately 600 seconds. This behavior is seen as a transition between two slopes in the logarithmic plots of 7, which are smoothed in the transition. This does not seem to be appropriate description at earlier times around
$\sim$ 50 seconds, where some electronic effects can significantly provoke deviations from the described patterns. For that reason, we select the fit to be
$f(t) = C\exp(\pm(t-t_0)/\tau)$, where t_0 is taken to be anywhere from 250 seconds to 400 seconds in 10 second intervals (500 seconds to 650 secods for 300K 1V). This range of values gives rise to a range of possible τ.

We argue that this extracted τ gives us the activation energy. Intuitively, we should expect this time constant to be inversely proportional to the drift velocity of the ions in the material, and since the the drift velocity is proportional to conductivity,

$$\tau \propto \frac{1}{\sigma} \propto k_B T \exp\left(\frac{E_A}{k_B T}\right), \tag{3}$$

and by plotting $\ln(\tau/T)$ vs $1/T$, the slope gives the activation energy.

Fig. 9 shows the activation energy measured with this method, $E_A = 0.083 \pm 0.009$ eV. This measurement is in very close agreement with predictions of theoretical studies [14, 34, 36] for $MAPbI_3$ and $MAPbBr_3$ halogen vacancy migration. We can attribute our results to ionic migration, but they cannot determine what ionic species or charge is migrating through our samples, although it is likely to be caused by either $V_{Br}^{\bullet}$ or Br^-.

IV. CONCLUSION AND FURTHER WORK

We have demonstrated major ion migration in $MAPbBr_3$ perovskites from room temperatures, 300 K, down to 140 K through SPCM measurements, mapping electrical fields to ionic effects on band bending. SPCM, then, can be utilized to extract activation energies of ions and their respective vacancies, and serves as a quantitative form of measurement for ion migration. We find an activation energy of $E_A = 0.083 \pm 0.009$ eV for a $MAPbBr_3$ microcrystal. While this value agrees with many theoretical predictions, it appears to be significantly smaller than many previous experimental investigations (with values of $\approx 0.15eV$ for polycrystaline films under light) on $MAPbBr_3$'s cousin, $MAPbI_3$ [28, 30, 44, 45].

We may explain our lower value by considering the microcrystal. It has been suggested that ion migration through a free surface is easier than through the bulk or a grain boundary given the lack of chemical bonds at such surface [28]. Our lack of a hole transporting layer (or any

other passive layer) allows the ions to easily move via the surface. The micron scale size of these pure crystals, also, contribute to a high surface to volume ratio, facilitating the transport.

Our measurement lacks a transition of activation energy between low and high temperatures often observed in literature [28, 30, 44, 45]. This might be mystified, whatsoever, by the small collection of temperature points. We suggest that more data points may be taken for a single crystal to make further conclusions.

Future ventures should investigate the species of ions or vacancies migrating though the material. Here, we suggest the use of a gate voltage modulation to change the concentrations of a certain species of ion in the surface before performing SPCM or KPFM. Similarly, an effort should be made towards passivisation or surface treatment of the perovskite, given that could reduce the exposed free surface area that allows or facilitates ion migration.

V. ACKNOWLEDGEMENTS

I would like to thank everyone who organized and participated in the REU experience alongside me, specially Rena Zieve, Nick Curro, and Daniel Cebra, but also everyone at Dong's Lab.

[1] Q. Dong, Y. Fang, Y. Shao, P. Mulligan, J. Qiu, L. Cao, and J. Huang, Electron-hole diffusion lengths greater than 175 μm in solution-grown $CH_3NH_3PbI_3$ single crystals, Science **347**, 967 (2015).

[2] M. A. Green, Y. Jiang, A. M. Soufiani, and A. Ho-Baillie, Optical properties of photovoltaic organic–inorganic lead halide perovskites, The journal of physical chemistry letters **6**, 4774 (2015).

[3] S. D. Stranks, G. E. Eperon, G. Grancini, C. Menelaou, M. J. Alcocer, T. Leijtens, L. M. Herz, A. Petrozza, and H. J. Snaith, Electron-hole diffusion lengths exceeding 1 micrometer in an organometal trihalide perovskite absorber, Science **342**, 341 (2013).

[4] J. Jeong, M. Kim, J. Seo, H. Lu, P. Ahlawat, A. Mishra, Y. Yang, M. A. Hope, F. T. Eickemeyer, M. Kim, *et al.*, Pseudo-halide anion engineering for α-$FAPbI_3$ perovskite solar cells, Nature **592**, 381 (2021).

[5] H.-Z. Berlin, World record back at HZB: Tandem solar cell achieves 32.5 percent efficiency (2022), last accessed 19 December 2022.

[6] E. J. Yoo, M. Lyu, J.-H. Yun, C. J. Kang, Y. J. Choi, and L. Wang, Resistive switching behavior in organic–inorganic hybrid $CH_3NH_3PbI_{3-x}Cl_x$ perovskite for resistive random access memory devices, Advanced Materials **27**, 6170 (2015).

[7] L. Protesescu, S. Yakunin, M. I. Bodnarchuk, F. Krieg, R. Caputo, C. H. Hendon, R. X. Yang, A. Walsh, and M. V. Kovalenko, Nanocrystals of cesium lead halide perovskites ($CsPbX_3$, X = Cl, Br, and I): novel optoelectronic materials showing bright emission with wide color gamut, Nano letters **15**, 3692 (2015).

[8] X. Wang, H. Liu, F. Zhou, J. Dahan, X. Wang, Z. Li, and W. Shen, Temperature gradient-induced instability of perovskite via ion transport, ACS applied materials & interfaces **10**, 835 (2018).

[9] D. Wei, H. Huang, P. Cui, J. Ji, S. Dou, E. Jia, S. Sajid, M. Cui, L. Chu, Y. Li, *et al.*, Moisture-tolerant supermolecule for the stability enhancement of organic–inorganic perovskite solar cells in ambient air, Nanoscale **11**, 1228 (2019).

[10] G. Richardson, S. E. O'Kane, R. G. Niemann, T. A. Peltola, J. M. Foster, P. J. Cameron, and A. B. Walker, Can slow-moving ions explain hysteresis in the current–voltage curves of perovskite solar cells?, Energy & Environmental Science **9**, 1476 (2016).

[11] J. Haruyama, K. Sodeyama, L. Han, and Y. Tateyama, First-principles study of ion diffusion in perovskite solar cell sensitizers, Journal of the American Chemical Society **137**, 10048 (2015).

[12] H. J. Snaith, A. Abate, J. M. Ball, G. E. Eperon, T. Leijtens, N. K. Noel, S. D. Stranks, J. T.-W. Wang, K. Wojciechowski, and W. Zhang, Anomalous hysteresis in perovskite solar cells, The journal of physical chemistry letters **5**, 1511 (2014).

[13] J. M. Frost, K. T. Butler, F. Brivio, C. H. Hendon, M. Van Schilfgaarde, and A. Walsh, Atomistic origins of high-performance in hybrid halide perovskite solar cells, Nano letters **14**, 2584 (2014).

[14] J. M. Azpiroz, E. Mosconi, J. Bisquert, and F. De Angelis, Defect migration in methylammonium lead iodide and its role in perovskite solar cell operation, Energy & Environmental Science **8**, 2118 (2015).

[15] Z. Xiao, Y. Yuan, Y. Shao, Q. Wang, Q. Dong, C. Bi, P. Sharma, A. Gruverman, and J. Huang, Giant switchable photovoltaic effect in organometal trihalide perovskite devices, Nature materials **14**, 193 (2015).

[16] E. J. Juarez-Perez, R. S. Sanchez, L. Badia, G. Garcia-Belmonte, Y. S. Kang, I. Mora-Sero, and J. Bisquert, Photoinduced giant dielectric constant in lead halide perovskite solar cells, The journal of physical chemistry letters **5**, 2390 (2014).

[17] S.-F. Zhang, X.-K. Chen, A.-M. Ren, H. Li, and J.-L. Bredas, Impact of organic spacers on the carrier dynamics in 2d hybrid lead-halide perovskites, ACS Energy Letters **4**, 17 (2018).

[18] L. D. Whalley, J. M. Frost, Y.-K. Jung, and A. Walsh, Perspective: Theory and simulation of hybrid halide perovskites, The Journal of chemical physics **146**, 220901 (2017).

[19] L. Shu, S. Ke, L. Fei, W. Huang, Z. Wang, J. Gong, X. Jiang, L. Wang, F. Li, S. Lei, *et al.*, Photoflexoelectric effect in halide perovskites, Nature materials **19**, 605 (2020).

[20] G. Y. Kim, A. Senocrate, T.-Y. Yang, G. Gregori, M. Grätzel, and J. Maier, Large tunable photoeffect on ion conduction in halide perovskites and implications for photodecomposition, Nature materials **17**, 445 (2018).

[21] E. Jedlicka, J. Wang, J. Mutch, Y.-K. Jung, P. Went, J. Mohammed, M. Ziffer, R. Giridharagopal, A. Walsh, J.-H. Chu, *et al.*, Bismuth doping alters structural phase transitions in methylammonium lead tribromide single crystals, The Journal of Physical Chemistry Letters **12**, 2749 (2021).

[22] K.-H. Wang, L.-C. Li, M. Shellaiah, and K. Wen Sun, Structural and photophysical properties of methylammonium lead tribromide ($MAPbBr_3$) single crystals, Scientific reports **7**, 1 (2017).

[23] S. Tao, I. Schmidt, G. Brocks, J. Jiang, I. Tranca, K. Meerholz, and S. Olthof, Absolute energy level positions in tin-and lead-based halide perovskites, Nature communications **10**, 1 (2019).

[24] G. Mannino, I. Deretzis, E. Smecca, A. La Magna, A. Alberti, D. Ceratti, and D. Cahen, Temperature-dependent optical band gap in $CsPbBr_3$, $MAPbBr_3$, and $FAPbBr_3$ single crystals, The journal of physical chemistry letters **11**, 2490 (2020).

[25] J. B. Goodenough, Electronic and ionic transport properties and other physical aspects of perovskites, Reports on Progress in Physics **67**, 1915 (2004).

[26] T.-Y. Yang, G. Gregori, N. Pellet, M. Grätzel, and J. Maier, The significance of ion conduction in a hybrid organic–inorganic lead-iodide-based perovskite photosensitizer, Angewandte Chemie **127**, 8016 (2015).

[27] D. W. DeQuilettes, W. Zhang, V. M. Burlakov, D. J. Graham, T. Leijtens, A. Osherov, V. Bulović, H. J. Snaith, D. S. Ginger, and S. D. Stranks, Photo-induced halide redistribution in organic–inorganic perovskite films, Nature communications **7**, 1 (2016).

[28] J. Xing, Q. Wang, Q. Dong, Y. Yuan, Y. Fang, and J. Huang, Ultrafast ion migration in hybrid perovskite polycrystalline thin films under light and suppression in single crystals, Physical Chemistry Chemical Physics **18**, 30484 (2016).

[29] M. H. Futscher, J. M. Lee, L. McGovern, L. A. Muscarella, T. Wang, M. I. Haider, A. Fakharuddin, L. Schmidt-Mende, and B. Ehrler, Quantification of ion migration in $CH_3NH_3PbI_3$ perovskite solar cells by transient capacitance measurements, Materials Horizons **6**, 1497 (2019).

[30] Y.-C. Zhao, W.-K. Zhou, X. Zhou, K.-H. Liu, D.-P. Yu, and Q. Zhao, Quantification of light-enhanced ionic transport in lead iodide perovskite thin films and its solar cell applications, Light: Science & Applications **6**, e16243 (2017).

[31] C. Eames, J. M. Frost, P. R. Barnes, B. C. O'regan, A. Walsh, and M. S. Islam, Ionic transport in hybrid lead iodide perovskite solar cells, Nature communications **6**, 1 (2015).

[32] R. A. De Souza and D. Barboni, Iodide-ion conduction in methylammonium lead iodide perovskite: some extraordinary aspects, Chemical Communications **55**, 1108 (2019).

[33] J. Mizusaki, K. Arai, and K. Fueki, Ionic conduction of the perovskite-type halides, Solid State Ionics **11**, 203 (1983).

[34] D. Barboni and R. A. De Souza, The thermodynamics and kinetics of iodine vacancies in the hybrid perovskite methylammonium lead iodide, Energy & Environmental Science **11**, 3266 (2018).

[35] R. De Souza, Oxygen diffusion in $SrTiO_3$ and related perovskite oxides, Advanced Functional Materials **25**, 6326 (2015).

[36] D. Meggiolaro, E. Mosconi, A. H. Proppe, R. Quintero-Bermudez, S. O. Kelley, E. H. Sargent, and F. De Angelis, Energy level tuning at the $MAPbI_3$ perovskite/contact interface using chemical treatment, ACS Energy Letters **4**, 2181 (2019).

[37] D. Yang, W. Ming, H. Shi, L. Zhang, and M.-H. Du, Fast diffusion of native defects and impurities in perovskite solar cell material $CH_3NH_3PbI_3$, Chemistry of Materials **28**, 4349 (2016).

[38] L. McClintock, Z. Song, H. C. Travaglini, R. T. Senger, V. Chandrasekaran, H. Htoon, D. Yarotski, and D. Yu, Highly mobile excitons in single crystal methylammonium lead tribromide perovskite microribbons, The Journal of Physical Chemistry Letters **13**, 3698 (2022).

[39] W. Melitz, J. Shen, A. C. Kummel, and S. Lee, Kelvin probe force microscopy and its application, Surface science reports **66**, 1 (2011).

[40] M. Salerno and S. Dante, Scanning kelvin probe microscopy: challenges and perspectives towards increased application on biomaterials and biological samples, Materials **11**, 951 (2018).

[41] R. Graham and D. Yu, Scanning photocurrent microscopy in semiconductor nanostructures, Modern Physics Letters B **27**, 1330018 (2013).

[42] J. Riviere, The work function of gold, Applied Physics Letters **8**, 172 (1966).

[43] Y. Hou, R. Xiao, S. Li, L. Wang, and D. Yu, Nonlocal chemical potential modulation in topological insulators enabled by highly mobile trapped charges, ACS Applied Electronic Materials **2**, 3436 (2020).

[44] D. Bryant, S. Wheeler, B. C. O'Regan, T. Watson, P. R. Barnes, D. Worsley, and J. Durrant, Observable hysteresis at low temperature in "hysteresis free" organic–inorganic lead halide perovskite solar cells, The Journal of Physical Chemistry Letters **6**, 3190 (2015).

[45] H. Yu, H. Lu, F. Xie, S. Zhou, and N. Zhao, Native defect-induced hysteresis behavior in organolead iodide perovskite solar cells, Advanced Functional Materials **26**, 1411 (2016).